Underground Space

The Role of the Plastic Zone Porosity and Permeability in Sand Production in Weak Sandstone Reservoirs

--Manuscript Draft--

Manuscript Number:	
Article Type:	Research Paper
Section/Category:	Geotechnical Engineering in Soft Ground
Keywords:	Sand production; Plastic zone; Weak sandstone; Porosity; Permeability
Corresponding Author:	Ainash Shabdirova Nazarbayev University Nur-Sultan, KAZAKHSTAN
First Author:	Ainash Shabdirova
Order of Authors:	Ainash Shabdirova
	Minh Nguyen, PhD
	Yong Zhao, PhD
Abstract:	Sand production is usually characterized as a two-stage process, where material failure occurs near the cavity leading to the formation of a plastic zone from which particles are detached and transported out due to a continuous hydrodynamic erosion under the effect of the produced fluid flow. The plastic zone porosity is affected by the coupled processes and the plastic zone permeability has an important impact on the performance of sand production prediction, especially in the weak sandstone reservoirs. Large-scale sand production experiments were conducted using a customized High-Pressure Consolidation Apparatus. The results show that specific stress-fluid pressure conditions may create the plastic zone around a hole, which has a decreased permeability compared to the intact zone. It was proposed that the plastic zone is composed of two subzones: high-permeable shear bands zone and low-permeable compaction zone. During sand production sand migrates from the compaction zone through shear bands zone to the perforation hole. Thus sand production is associated with the permeability and porosity increase in the compaction zone. The existing sand prediction models were modified according to the new findings and the modified model showed better performance. The modified model was validated by the sanding data from weak sandstone reservoir in Kazakhstan.
Suggested Reviewers:	Alireza Nouri anouri@ualberta.ca Dr. Alireza Nouri has research expertise in sand production area.
	Pei-Chen Wu peichen.wu@connect.polyu.hk Dr. Wu has conducted experiments on soils and rocks.
Opposed Reviewers:	

Dear editor,

We are submitting a manuscript for consideration of publication in Underground Space. The title of the manuscript is "The Role of the Plastic Zone Porosity and Permeability in Sand Production in Weak Sandstone Reservoirs".

It has not been published elsewhere and has not been submitted simultaneously for publication elsewhere.

This paper presents an analytical and semi-empirical model for sand production prediction. The novelty of the model consists in introducing plastic zone porosity and permeability concept to the existing sanding rate models. The experimental works and analytical study show that plastic zone permeability decrease, which is contrary to the previous models.

The model was calibrated by experimental sand production data, and validated by field sand production data. The results of this study might be interesting for further experimental research on sanding rate predictions and weak sandstone mechanics.

Thank you for the consideration of the manuscript for publication in Underground Space.

Sincerely,

Authors.

Title Page (with Author Details)

Title: The Role of the Plastic Zone Porosity and Permeability in Sand Production in Weak Sandstone Reservoirs

Authors: Ainash Shabdirova[a]*, Nguyen Hop Minh[b], Yong Zhao[a]

[a] School of Engineering and Digital Sciences, Nazarbayev University, Nur-Sultan, Kazakhstan
[b] Fulbright University Vietnam, Ho Chi Minh City, Vietnam

emails: ainash.shabdirova@nu.edu.kz

yong.zhao@nu.edu.kz

hopminh2003@gmail.com

The Role of the Plastic Zone Porosity and Permeability in Sand Production in Weak Sandstone Reservoirs

Ainash Shabdirova[a]*, Nguyen Hop Minh[b], Yong Zhao[a]

[a] *School of Engineering and Digital Sciences, Nazarbayev University, Nur-Sultan, Kazakhstan*
b Fulbright University Vietnam, Ho Chi Minh City, Vietnam

Abstract

Sand production is usually characterized as a two-stage process, where material failure occurs near the cavity leading to the formation of a plastic zone from which particles are detached and transported out due to a continuous hydrodynamic erosion under the effect of the produced fluid flow. The plastic zone porosity is affected by the coupled processes and the plastic zone permeability has an important impact on the performance of sand production prediction, especially in the weak sandstone reservoirs. Large-scale sand production experiments were conducted using a customized High-Pressure Consolidation Apparatus. The results show that specific stress-fluid pressure conditions may create the plastic zone around a hole, which has a decreased permeability compared to the intact zone. It was proposed that the plastic zone is composed of two subzones: high-permeable shear bands zone and low-permeable compaction zone. During sand production sand migrates from the compaction zone through shear bands zone to the perforation hole. Thus sand production is associated with the permeability and porosity increase in the compaction zone. The existing sand prediction models were modified according to the new findings and the modified model showed better performance. The modified model was validated by the sanding data from weak sandstone reservoir in Kazakhstan.

Keywords: Sand production; Plastic zone; Weak sandstone; Porosity; Permeability

1. Introduction

Weak shallow oil reservoirs are usually prone to sand production and the produced sand can lead to additional costs due to equipment failure, well shutdown, and environmental contamination.

The sand production phenomenon can be considered as a two-stage process: first, the material around a borehole fails when stresses exceed the material's strength; second, disaggregation and transportation of the failed material happen due to fluid flow.

Sanding onset prediction is based on formulating stress solutions near the hole and applying failure criteria to these stresses, therefore constitutive material model and failure criterion are required. The sanding onset condition has been studied in detail and is well predicted for most field cases (Morita et al., 1989; Wu et al., 2006; Kessler et al., 2007; Weingarten and Perkins, 2007; Wang and Dusseault, 2010; Han et al., 2011; Al-Shaaibi et al., 2013; Fuh and Morita, 2013; Araujo et al., 2014; Papamichos and Furui, 2013; 2019). The most common material model used to study sand production is a linear poroelastoplastic model (Al-Shaaibi et al., 2013; Hayavi & Abdideh, 2017; Morita, Whitfill, Massie, & Knudsen, 2007; Papamichos, Vardoulakis, Tronvoll, & Skjaerstein, 2001; H. Wang & Sharma, 2017; Yi, 2003). The model describes the mechanical

behaviour of porous media in terms of the effective stresses: the applied stresses are carried by the solid skeleton and the fluid inside the pores. When the applied effective stresses exceed the material strength, it is considered to fail and changes its state from elastic to plastic. A zone of material undergoing plastic deformation is formed around the cavity and failure occurs when a shear failure criterion is satisfied in terms of the stress distribution in the plastic zone and this is dependent on the flow characteristics in terms of the fluid flow rate and rock permeability. Linear Mohr-Coulomb is the simplest failure criterion, which states that shear failure depends only on the minimum and maximum principal stresses (Fjaer, Holt, Horsrud, Raaen, & Risnes, 1993):

$$\tau = S_0 + \mu\sigma' \tag{1}$$

Despite its simplicity Mohr-Coulomb criterion is successfully employed to predict sanding onset for some fields (Yi, 2003; Hayavi & Abdideh, 2017).

As the stresses around the cavity increase and fulfil the failure criterion, the material transforms from elastic to a plastic state. Bratli and Risnes (1981) determined a plastic zone of the failed materials around a sand arch after a shear failure. First, the in-situ stresses near the sand arch are calculated. The greatest difference between the stresses was found to occur at the inner surface, and this region fails first. The material behaves elastically up to the limit given by the Mohr-Coulomb failure criterion. Risnes et al. (1982) extended the work through the investigation of the stresses around the open borehole and cased-hole completions. Following these studies, the formation of the plastic zone had been reported in several experimental and numerical studies (Goshtasbi, Elyasi, & Naeimipour, 2013; Tronvoll & Fjær, 1994; H. Wang & Sharma, 2017).

Literature review on the plastic zone permeability showed limited and contradicting results; it could be a varying value across the plastic zone in Bratli and Risnes (1981), or a single value of one-tenth of the intact zone permeability in Risnes et al. (1982).

Permeability alteration in the near-borehole area can be the result of both stress changes around hole and invasion of particles during hole creation. Daigle et al. (2017) developed a numerical model of the depleted North Sea reservoir to show the permeability reduction in the near-wellbore area. The authors explain this compaction as a result of the increase in effective stresses in the reservoir.

Cuss et al. (2003) experimentally observed porosity reduction near the borehole wall and borehole breakouts during hydrostatic loading due to stress concentration. Han and Dusseault (2003) analytically estimated the stress-dependent porosity and permeability in the plastic zone defined by the Mohr-Coulomb shear failure around a wellbore and concluded that for unconsolidated sandstones the reduction is negligible. Their conclusion contradicts with other experimental investigations of the stress-dependent permeability in weak porous sandstones (Holt, 1990; Sarda, Ferfera, Vincké, Boutéca, & Longuemare, 1988), where permeability reduction was more than 50%.

Zhu and Wong (1997) studied the transition from brittle failure to cataclastic flow and discovered that for porous sandstones the permeability decreases before peak stress is reached. Tovar et al. (2007) described this permeability reduction as geomechanical damage and introduced a methodology for quantification of a skin factor due to the combined action of geomechanical damage and fluid invasion damage. On the other hand, as it was mentioned above, weak rocks are characterized by slip lines breakout mode, which forms shear bands with high permeability around

the hole. Hollow-cylinder experiments and numerical modelling conducted by Cerasi et al. (2005) showed that the shear bands do not extend throughout the whole plastic zone, but concentrated near the borehole.

Arora and Sharma (2000) developed a model to understand the factors controlling the permeability distribution around a perforation tunnel. They conclude that during underbalance perforating, the permeability around the perforation is controlled by fines generated by the shock wave and by fines transported during surge flow back into the wellbore. They determined high-permeable region of the failed material immediately near perforation due to the fractures. This region is followed by the compaction zone, which is consists of the crushed and squeezed sand particles.

In the more recent work by Khamitov et al. (2020) the sand production is studied using the coupled DEM-CFD model. The authors presented the porosity distribution around the perforation hole with radius r, where there was a high-porosity zone near the perforation tunnel in the radial distance between r and $2r$ and low-porosity zone between $2r$ and $5r$.

As can be seen, a few controversial studies were conducted on the properties of the plastic zone around a hole in a weak sandstone. At the same time, the plastic zone is a very important part of the sand production models. In the current study, sand production experiments were conducted on a customized apparatus to study the porosity and permeability distribution in the plastic zone. The new findings were incorporated into the existing sand prediction models (Papamichos et al., 2001; Paul Jacob van den Hoek & Geilikman, 2003) to demonstrate the importance of the plastic zone properties. The modified models were used to predict sanding data from the oil field in the Ustuyrt-Buzachi Sedimentary Basin in Kazakhstan. This study aims to show the significance of the plastic zone porosity and permeability distribution in the sand production prediction.

A sensitivity analysis of the sand volume prediction model for weak sandstone reservoirs in Kazakhstan presented by Shabdirova et al. (2019) suggested that the plastic zone permeability has a strong impact on the prediction. This paper presents a further development of the model by Shabdirova et al. (2019). The reservoir rock of the oil field in the Ustuyrt-Buzachi Sedimentary Basin consists of shallow marine sandstones of Lower Cretaceous age deposited at 200 - 500 m depth. The sandstones are mainly composed of fine quartz and feldspar particles cemented with clay minerals. The average particle size of the reservoir varies from horizon to horizon in the range of 0.25-0.3 mm. The reservoir is characterized as porous (porosity of up to 38%), permeable (permeability between 100 and 800 mD), and weak (Dobereiner & Freitas, 1986). The core samples from the field were of very poor quality and insignificant volume for mechanical testing in the laboratory. The reservoir fluid has a very high viscosity, between 200 – 800 mPa·s. Current reservoir pressure varies from 2 to 3 MPa. The reservoir pressure maintenance is carried out by water flooding, and as a result wells in the sectors with 3 MPa reservoir pressure produce high water cut (minimum 60%). Due to the low strength of the reservoir rock, the producing zone is cased and perforated with a density of 16 shots per meter. For most wells it was observed that the initial sand burst during the well startup is followed by a reduction in sand rate down to zero at the constant flow rate. Further increase in production may cause a new surge of sand. The modified model developed in this study was validated against the production data of 40 wells from the oil field and its potential efficiency was proven in case appropriate amendments will be made to the model based on more realistic assumptions.

2. Development of a sanding prediction model for weak sandstone reservoir

Sand production is usually characterized as a two-stage process: 1) formation of a plastic zone surrounding the cavity that can be predicted with the reservoir material being assumed as a poroelastoplastic material; 2) erosion of the failed material from the plastic zone under the effect of the produced fluid flow. The model is developed based on the assumption of a shear failure model, a flow model, an erosion model, and a material model.

2.1. Shear failure model for the formation of the plastic zone

Consider an isotropic and homogenous cylindrical sample with a central through-hole (Figure 1). R_i is a hole radius, R_o is an outer boundary radius.

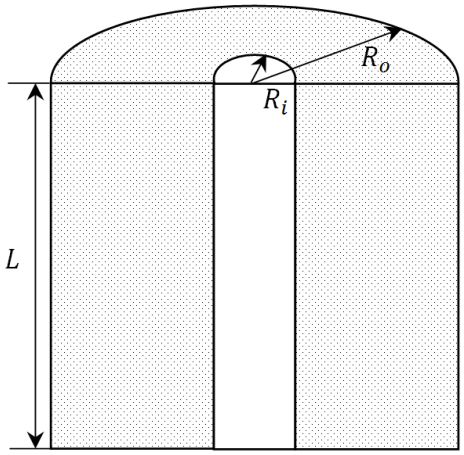

Figure 1. Cylindrical sample with a central hole.

The poroelastoplastic material model is employed to determine the stress distributions around the hole, which is considered to adequately represent weak porous formations in sand production studies (Al-Shaaibi et al., 2013; Hayavi & Abdideh, 2017; Morita et al., 2007; Papamichos et al., 2001; H. Wang & Sharma, 2017; Yi, 2003). The cylindrical geometry of a perforation tunnel is presented in Fig. 1 with an outer boundary radius of R_o and an inner hole radius of R_i. Stresses in the intact zone can be found as follows (Risnes et al., 1982):

$$\sigma_r = \sigma_h + (\sigma_h - p_i)\frac{R_i^2}{R_o^2 - R_i^2}\left[1 - \frac{R_o^2}{r^2}\right] - (p_o - p_i)\eta\left\{\frac{R_i^2}{R_o^2 - R_i^2}\left[1 - \frac{R_o^2}{r^2}\right] + \frac{\ln\frac{R_o}{r}}{\ln\frac{R_o}{R_i}}\right\} \quad (2)$$

$$\sigma_\theta = \sigma_h + (\sigma_h - p_i)\frac{R_i^2}{R_o^2 - R_i^2}\left[1 + \frac{R_o^2}{r^2}\right] - (p_o - p_i)\eta\left\{\frac{R_i^2}{R_o^2 - R_i^2}\left[1 + \frac{R_o^2}{r^2}\right] + \frac{\ln\frac{R_o}{r} - 1}{\ln\frac{R_o}{R_i}}\right\} \quad (3)$$

$$\sigma_z = \sigma_v + 2\nu_{fr}(\sigma_h - p_i)\frac{R_i^2}{R_o^2 - R_i^2} - (p_o - p_i)\eta\left\{\frac{2\nu_{fr}R_i^2}{R_o^2 - R_i^2} + \frac{2\ln\frac{R_o}{r} - \nu_{fr}}{\ln\frac{R_o}{R_i}}\right\} \quad (4)$$

where σ_r – radial stress at distance r from the hole axis, σ_h - far-field minimum horizontal stress, p_i – fluid pressure on the hole wall, R_i – inner radius, R_o – an outer radius of the boundary, p_o – fluid pressure at the outer boundary, η – compressibility constant, σ_θ - tangential stress at

distance r from the perforation axis, ν_{fr} – Poisson's ratio, σ_z – axial stress at distance r from the perforation axis, σ_v – far-field vertical stress. The far-field stress is assumed to be the same in Eqs. (2) – (4).

The plastic zone around the perforation is formed when the stresses satisfy a shear failure condition, of which the Mohr-Coulomb criterion can be applied in this study. Stresses in the plastic zone are given as in Risnes et al. (1982):

$$\sigma_r = p_i + \frac{\mu q}{2\pi L k_p} ln\left(\frac{r}{R_i}\right) + \frac{1}{tt}\left(2S_0 tan\alpha - \frac{\mu q}{2\pi L k_p}\right)\left[\left(\frac{r}{R_i}\right)^{tt} - 1\right] \quad (5)$$

$$\sigma_\theta = p_i + \frac{\mu q}{2\pi L k_p}\left(1 + ln\left(\frac{r}{R_i}\right)\right) + \frac{1}{tt}\left(2S_0 tan\alpha - \frac{\mu q}{2\pi L k_p}\right)\left[(tt+1)\left(\frac{r}{R_i}\right)^{tt} - 1\right] \quad (6)$$

$$\sigma_z = p_i + \frac{\mu q}{2\pi L k_p}\left(1 + ln\left(\frac{r}{R_i}\right)\right) + \frac{1}{tt}\left(2S_0 tan\alpha - \frac{\mu q}{2\pi L k_p}\right)\left[(tt+1)\left(\frac{r}{R_i}\right)^{tt} - 1\right] \quad (7)$$

where q – the flow rate in the radial direction, μ – fluid viscosity, L – perforation length, k_p – permeability of plastic zone, α – failure angle, S_0 - inherent shear strength, and $tt = tan^2\alpha - 1$.

The radius of the plastic zone can be found when the stress distributions inside the intact zone and the plastic zone satisfy the Mohr-Coulomb criterion at the interface between two zones, which can be described in terms of the tangential principal stress in the intact zone (σ'_{1e}) and the radial principal stress in the plastic zone (σ'_{3p}) in Eq.8. The plastic zone radius R_p can be found knowing the stress values, flow rate, and plastic zone permeability k_p:

$$\sigma'_{1e} = 2S_0 tan\alpha + \sigma'_{3p} tan^2\alpha \quad (8)$$

where σ'_{1e} - maximum principal stress in the intact zone, σ'_{3p} – minimum principal stress in the plastic zone. Note that while Eq.8 allows the determination of R_p, the calculation requires the knowledge of the plastic zone permeability, k_p, which can be found from the flow model in the following section.

2.2. Flow model across the intact zone and plastic zone

If we assume that the applied stresses and fluid pressures result in the formation of the plastic zone around a hole with the yet unknown radius and permeability, the cylindrical sample will look like as in Figure 2.

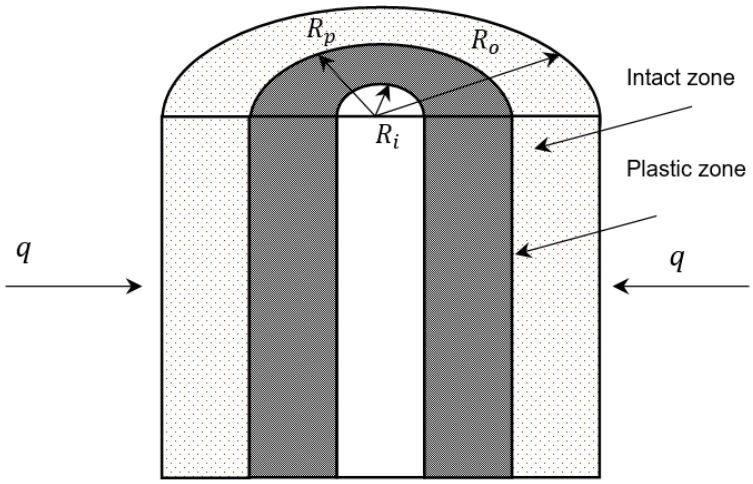

Figure 2. The plastic zone around a hole in a cylindrical sample.

Plastic zone permeability k_p and plastic zone radius R_p can be related to the intact zone permeability k, inner radius R_i, and outer boundary radius R_o through the average permeability of the sample k_{avg}. Consider the radial flow through a sample with two layers of different permeability of the plastic and intact zones (Figure 2).

The plastic zone permeability can be expressed as:

$$k_p = \frac{k_{avg} k \ln\frac{R_p}{R_i}}{k \ln\frac{R_o}{R_i} - k_{avg} \ln\frac{R_o}{R_p}} \tag{9}$$

The average permeability k_{avg} can be determined from a radial flow experiment on a hollow cylinder sample as similar to the geometry in Figure 2 using Darcy's law knowing the values of the applied drawdown ($\Delta p = p_o - p_i$) and of the measured fluid flow rate:

$$k_{avg} = \frac{q\mu \ln\frac{R_o}{R_i}}{2\pi h L \Delta p} \tag{10}$$

Knowing the value of k_{avg} would allow us to calculate the plastic zone permeability, k_p, in Eq.9, which on the other hand allows us to calculate R_p from the shear failure model Eq.8.

The hole failure mode in weak sandstones is characterized by the formation of shear bands (B. Wu & Choi, 2012; Bailin Wu et al., 2016; Yan et al., 2020). We propose that the formation of shear bands is accompanied by squeezing of the sample material behind the shear bands outward to the sample periphery due to stress redistributions. Thus, there is a low-permeable compaction zone right after the high-permeable shear bands zone. This proposition can be supported by several other studies (Arora & Sharma, 2000; Khamitov, Minh, & Zhao, 2020b).

Following our approach, a cylindrical sample in Figure 2 can be modified as in Figure 3 to capture the new zone.

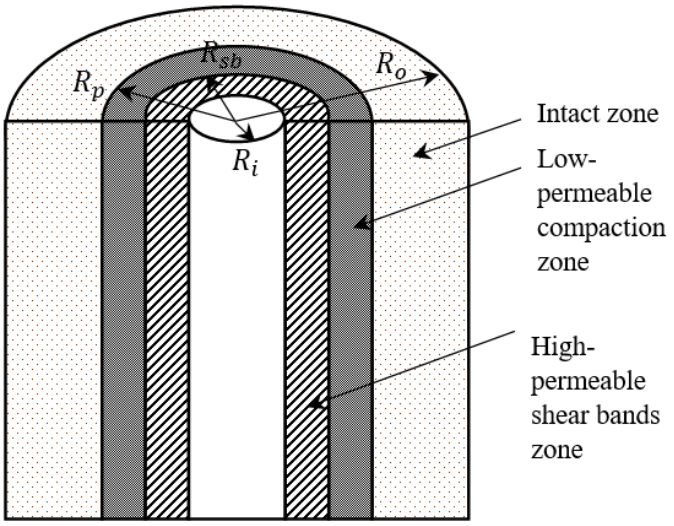

Figure 3. Shear bands zone and low-permeable compaction zone.

If we follow the idea of fluid flow across the plastic and intact zones presented above, the average permeability of the sample in case of radial flow can be written as:

$$k_{avg} = \frac{\ln\frac{R_o}{R_i}}{\frac{\ln\frac{R_{sb}}{R_i}}{k_{sb}} + \frac{\ln\frac{R_p}{R_{sb}}}{k_c} + \frac{\ln\frac{R_o}{R_p}}{k}} \tag{11}$$

where R_{sb} – the radius of the shear bands zone, R_p – the plastic zone radius, k_{sb} – the permeability of the shear bands zone, k_c – the compaction zone permeability.

Thus, the shear bands zone, which width is $(R_{sb} - R_i)$, has high permeability. On the other hand, the compaction zone with width $(R_p - R_{sb})$ has low permeability. As a result, the average permeability of the sample decreases compared to the intact permeability. Change of flow rate produces a new redistribution of stresses and alteration of radius and permeability of the shear bands and compaction zones, which in turn changes average permeability. Knowledge of the properties of these zones can be important for estimation of sand production.

Based on the above observation, discussions in the literature on the stress-induced compaction (Cuss et al., 2003; G. Han, Dusseault, & Cook, 2002; Holt, 1990; Raghavan, Chin, & Company, 2002; Risnes et al., 1982; Sarda et al., 1988; Zhu & Wong, 1997) and shear bands around a hole in weak rocks (Arora & Sharma, 2000; Khamitov et al., 2020b; Papamichos, Skjaerstein, & Tronvoll, 2000; B. Wu & Choi, 2012; Bailin Wu et al., 2016; Yan et al., 2020), we propose the following evolution of the plastic zone around a hole depending on the applied stresses and fluid pressures. At the very beginning, just after a hole creation, there is a compaction zone (Figure 4a) around the hole due to the stress redistribution and invasion of the broken particles. Thickness, permeability and porosity of this zone depend on the applied stresses and penetration method. Further stress conditions create shear bands and the compaction front moves away from the hole (Figure 4b). Properties of the shear bands and compaction zones may change with changing stress conditions (Figure 4c).

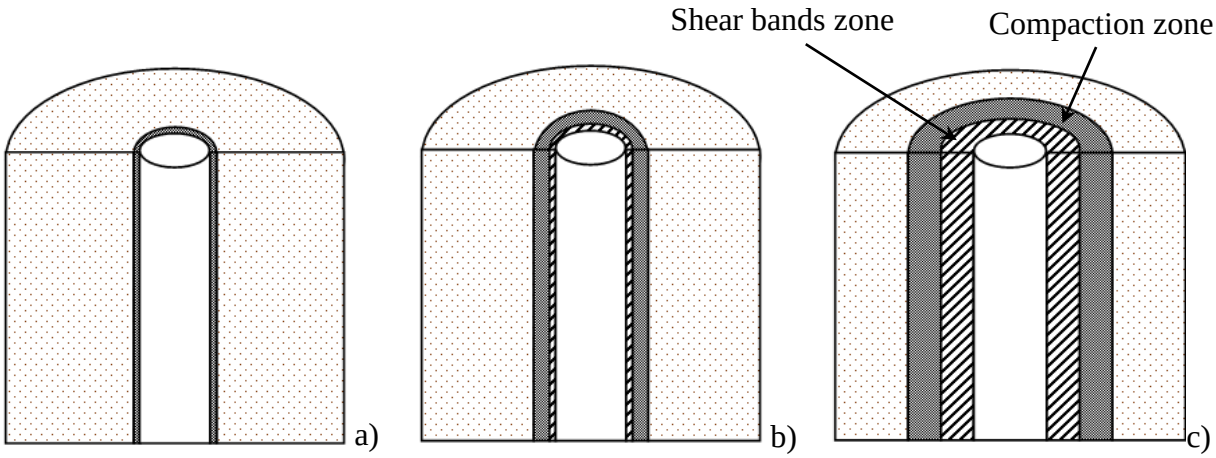

Figure **Error! No text of specified style in document.**. Shear bands and compaction zones around a hole: a) just after hole creation, only compaction zone; b) shear bands zone is formed and compaction zone moves; c) properties of the zones change with the stress conditions.

Introduction of the fluid flow may contribute to the enlargement of the plastic zone and its further compaction until some critical value. Once the fluid rate exceeds this value sand particles start to migrate from the compaction zone towards shear bands zone and the perforation hole. For better perception let us illustrate the above discussions in terms of porosity change in the different zones. We assume a linear relationship between porosity and permeability given by Kozeny-Carman equation (Carman, 1939; Kozeny, 1927):

$$k = k_0 \frac{\phi^3}{(1-\phi)^2} \tag{12}$$

where k_0 – permeability constant, which accounts for the effects of particle size and tortuosity of the sample.

Let us consider the state just before the sand production initiation. We divide the plastic zone into two equal zones for simplicity. In fact, dimensions of the zones might be different. The first zone is a shear bands zone and the second is a compaction zone. If we impose cross-section of the quarter of the cylindrical sample on top of the porosity vs distance graph, we can illustrate high-permeable shear bands zone, low-permeable compaction zone, and intact zone (Figure 5) at state *A* before sand production.

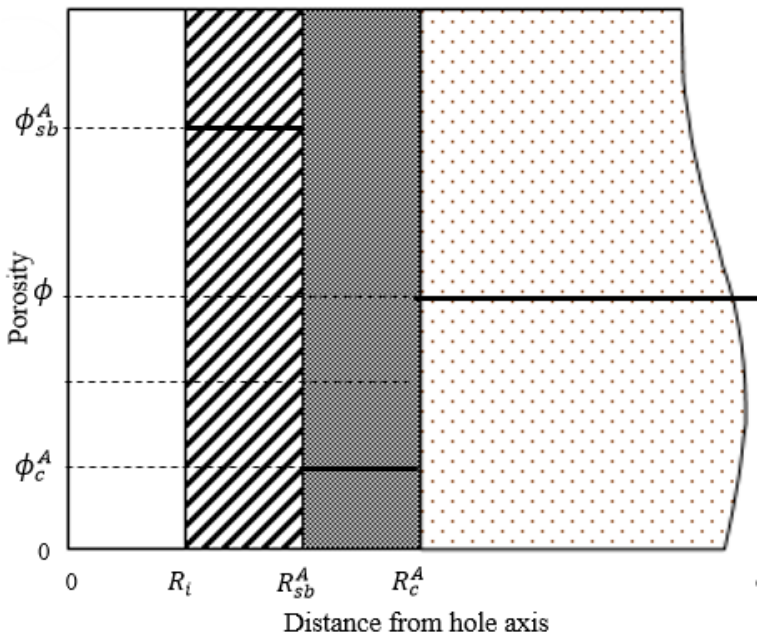

Figure 5. Subzones of the plastic zone with different porosity.
Before sand production.

Once the fluid rate exceeds the critical value, it detaches and transports sand particles from the compaction zone to the shear bands zone and perforation hole. This means porosity in the compaction zones increase due to particles moving out, and porosity in the shear bands zone decrease due to particles moving in. Note that radiuses of the subzones also change with increasing flow rate.

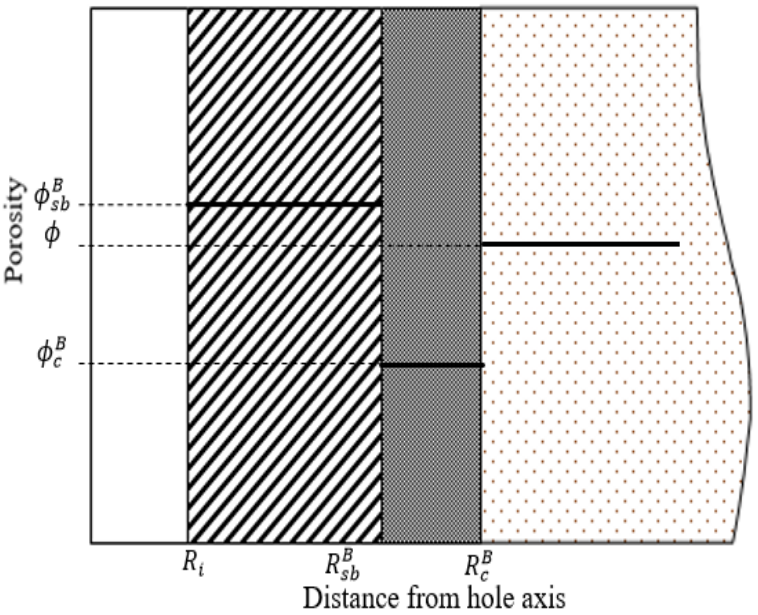

Figure 6. Subzones of the plastic zone. After sand production.

Figure 6 shows one of the possible porosity change scenarios after sand production. For simplicity of calculations, this scheme will be used to estimate porosity distribution during sand production experiments. Thus, we can see that the shear bands zone enlarges and the compaction zone moves away from the hole. Porosity in the shear bands zone may decrease due to sand migration and porosity in the compaction zone increases due to the sand production and the compaction zone at state *A* turns into shear bands zone at state *B*. Superscripts *A* and *B* stand for states where *A* – before sand production, and *B* – after sand production.

k_p is the average permeability across the plastic zone, so in analogy to the above flow model we can write the following equation:

$$k_p = \frac{\ln\frac{R_p}{R_i}}{\frac{\ln\frac{R_{sb}}{R_i}}{k_{sb}} + \frac{\ln\frac{R_p}{R_{sb}}}{k_c}} \tag{13}$$

At state *A*, if we assume that all the excess sand mass in the compacted zone were squeezed from the shear bands zone, we can write the mass balance equation:

$$m_{sb} = m_c \tag{14}$$

At state *B*, part of the excess sand mass is migrated from the compaction zone and produced:

$$m_{sb} = m_c + m \tag{15}$$

here

$$m_{sb} = \pi L(R_{sb}^2 - R_i^2)(\phi_{sb} - \phi)\rho \tag{16}$$

$$m_c = \pi L\left(R_p^2 - R_{sb}^2\right)(\phi - \phi_c)\rho \tag{17}$$

where m_{sb} – sand mass squeezed from the shear bands zone towards compaction zones, m_c – sand mass squeezed into the compaction zone, m – mass of the produced sand, L – sample height, R_{sb}, R_p – the radiuses of the shear bands zone and the plastic zone, respectively; ρ – sand particle density; ϕ, ϕ_{sb}, ϕ_c – porosity values of the intact zone, shear bands zone, and the compaction zone, respectively. These porosity values can be expressed in terms of the corresponding permeability value following from the Kozeny-Carman equation:

$$\phi_{sb} = \sqrt[3]{\left(\frac{1}{27}\cdot\left(\frac{k_{sb}}{k_0}\right)^3-\frac{1}{3}\cdot\left(\frac{k_{sb}}{k_0}\right)^2+\frac{1}{2}\cdot\frac{k_{sb}}{k_0}\right)+\sqrt{\left(\frac{1}{27}\cdot\left(\frac{k_{sb}}{k_0}\right)^3-\frac{1}{3}\cdot\left(\frac{k_{sb}}{k_0}\right)^2+\frac{1}{2}\cdot\frac{k_{sb}}{k_0}\right)^2+\left(\frac{2k_{sb}}{3k_0}-\frac{1}{9}\cdot\left(\frac{k_{sb}}{k_0}\right)^2\right)^3}} + \sqrt[3]{\left(\frac{1}{27}\cdot\left(\frac{k_{sb}}{k_0}\right)^3-\frac{1}{3}\cdot\left(\frac{k_{sb}}{k_0}\right)^2+\frac{1}{2}\cdot\frac{k_{sb}}{k_0}\right)-\sqrt{\left(\frac{1}{27}\cdot\left(\frac{k_{sb}}{k_0}\right)^3-\frac{1}{3}\cdot\left(\frac{k_{sb}}{k_0}\right)^2+\frac{1}{2}\cdot\frac{k_{sb}}{k_0}\right)^2+\left(\frac{2k_{sb}}{3k_0}-\frac{1}{9}\cdot\left(\frac{k_{sb}}{k_0}\right)^2\right)^3}} + \frac{k_{sb}}{3k_0}$$

$$\phi_{c} = \sqrt[3]{\left(\frac{1}{27}\cdot\left(\frac{k_{c}}{k_0}\right)^3-\frac{1}{3}\cdot\left(\frac{k_{c}}{k_0}\right)^2+\frac{1}{2}\cdot\frac{k_{c}}{k_0}\right)+\sqrt{\left(\frac{1}{27}\cdot\left(\frac{k_{c}}{k_0}\right)^3-\frac{1}{3}\cdot\left(\frac{k_{c}}{k_0}\right)^2+\frac{1}{2}\cdot\frac{k_{c}}{k_0}\right)^2+\left(\frac{2k_{c}}{3k_0}-\frac{1}{9}\cdot\left(\frac{k_{c}}{k_0}\right)^2\right)^3}} + \sqrt[3]{\left(\frac{1}{27}\cdot\left(\frac{k_{c}}{k_0}\right)^3-\frac{1}{3}\cdot\left(\frac{k_{c}}{k_0}\right)^2+\frac{1}{2}\cdot\frac{k_{c}}{k_0}\right)-\sqrt{\left(\frac{1}{27}\cdot\left(\frac{k_{c}}{k_0}\right)^3-\frac{1}{3}\cdot\left(\frac{k_{c}}{k_0}\right)^2+\frac{1}{2}\cdot\frac{k_{c}}{k_0}\right)^2+\left(\frac{2k_{c}}{3k_0}-\frac{1}{9}\cdot\left(\frac{k_{c}}{k_0}\right)^2\right)^3}} + \frac{k_{c}}{3k_0}$$

By solving the system of Eqs. 13-15 we can estimate porosity and permeability distribution in the plastic zone and mass of the produced sand, which can be found as a difference between the masses in the regions where porosity increases and the regions where porosity decreases. The proposed approach is applied to the sand production experiments described in the following section.

3. Experimental results and discussions

3.1 High-Pressure Consolidation System for sand production experiments

In all the existing experimental studies on sand production (Fattahpour, Moosavi, & Mehranpour, 2011, 2012; Nouri, Vaziri, Belhaj, & Islam, 2006; Papamichos et al., 2001; Anne Skjaerstein, Tronvoll, Santarelli, & Joranson, 1997; P.J. van den Hoek et al., 2007; B. Wu & Choi, 2012), the sample is prepared outside and then transported into the sand production apparatus. This may cause disturbance to the sample. In addition, in most cases, several samples are prepared before the test and tested in succession so that the properties of the samples tested later may change with time, which affects the experimental results and reproducibility of the tests. A new apparatus was designed for the sand production experiment to allow for three processes of sandstone diagenesis, perforation and fluid production to take place on the same sandstone specimen to minimize disturbance and to replicate the field condition in the laboratory. The so-called High-

Pressure Consolidation System (HPCS) as shown in Figure 7 consists of a load frame (1) with a hydraulic actuator at the bottom (2), a specimen cell (4), an actuator's control unit (5) and data acquisition (6), a fluid pump (7), fluid pump's valves (8) and control (9), a fluid tank (10). Large specimen of 220 mm in height and 300 mm in diameter can be prepared and tested. Larger specimen sizes benefit from excluding boundary effects in the experimental results.

Figure 7. High-Pressure Consolidation System.

The system can apply a maximum axial vertical load of 5000 kN, which is equivalent to a maximum reservoir depth of around 3200 m. Servo-hydraulic mechanism inside the actuator (2) pushes the pedestal and the cell on top of it against top cap and load frame. Thus, an axial load is applied by compressing the sample from the bottom. Stress control or strain control modes can be activated depending on the test conditions.

Load transducer is placed inside the control unit (5) and measures the oil pressure required to lift the cell (Figure 8a). This pressure value is automatically converted to the load using the specimen area. Displacement transducer is attached to the actuator from the outside (Figure 8b) and controls the position of the pedestal.

a)

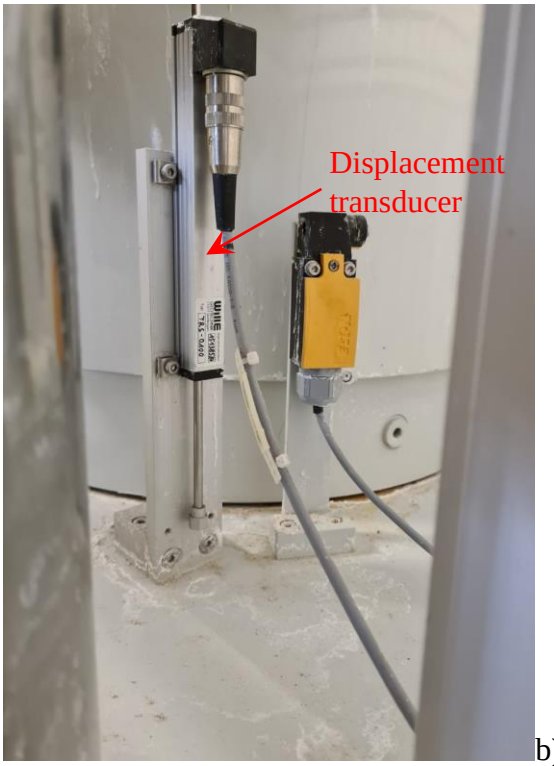

b)

Figure 8. The load and displacement transducers.

The specimen is connected in a series to a top cap, a top plunger to the load frame on the top. The fluid flow of up to 5 l/min or under a maximum inlet pressure of 7 MPa can be injected through eight inlet ports located on the cell wall and/or two ports at the bottom (Figure 9a). The outflow is made available through a central hole on the top cap to the inner space inside the top plunger and to an outlet on the side of the plunger. The outlet pressure gauge and mass flowmeter are installed at the back end of the outlet tube (Figure 9b), before the outlet valve and after the filter which is designed to pass sand particles less than 0.4 mm and protect the transducer and flowmeter from the large sand clusters. There are also additional valves for cleaning and bypassing purposes. Radial stress transducers and ultrasonic sensors are installed in the inner wall of the cell to develop direct contact with the specimen. Pore pressure transducer is located at the bottom of the specimen and its surface is covered with the filter paper to protect the piezoresistive element inside the transducer from sand particles.

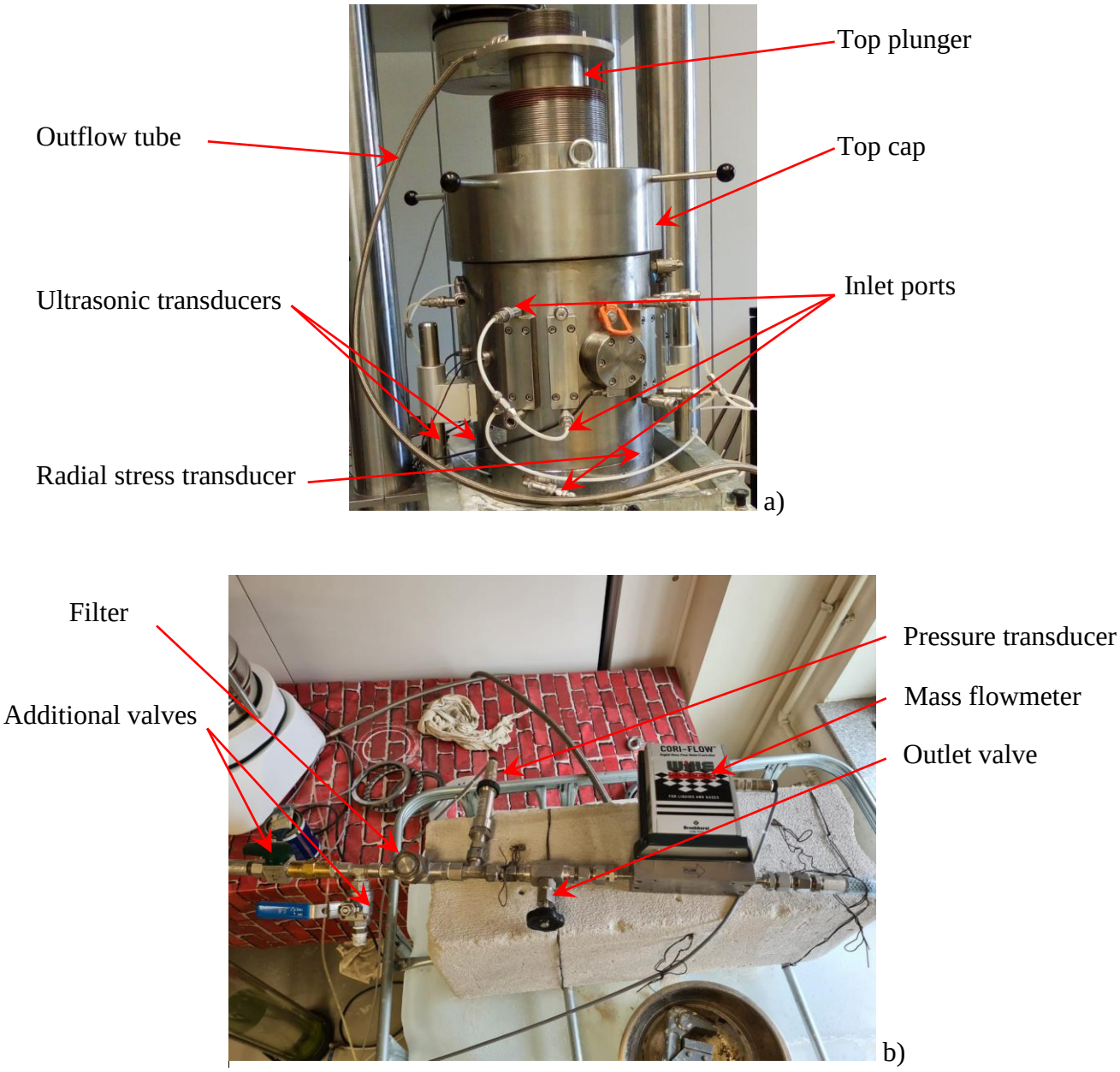

Figure 9. High-Pressure Consolidation Cell.

Fluid pump unit and its valve station are used to distribute and control water and CO_2 flow (Figure 10). The valve station has six valves: four valves for the radial ports and two valves for the top and bottom ports. Inlet tubings connect the valve station with the inlet ports. A vertical position of the valves indicates the closed condition. The fluid flows into the cell when the valve is on the “FILL” position and flows from the cell when the position is on the “DRAIN”. Fluid pump can be controlled from the software or manually using the operator panel on the pump. The software allows both fluid rate and inlet pressure control, while only the flow rate can be set using the operator panel. The fluid pump unit can be connected to two reservoirs with a different fluid.

The upper red handle is used to switch between the reservoirs. In the current study, only water was injected, and therefore the upper handle was turned to the left. The lower handle is used to choose how to inject the fluid: turned to the right - using the pump itself; or turned to the left - connect to the outer pressure source. Thus, when we injected CO_2 from the pressurized gas balloon, the lower red handle was turned to the left, and when we injected water – to the right.

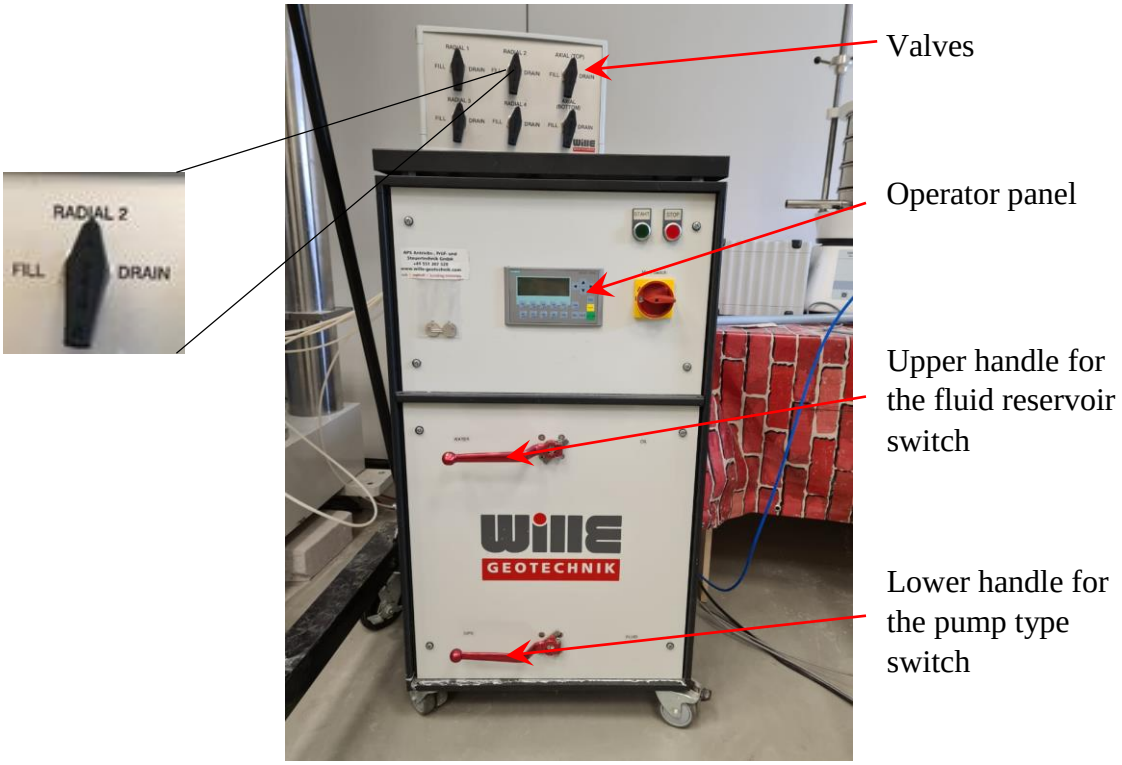

Figure 10. Fluid pump unit and its valve station.

Artificial specimens were prepared to match the reservoir sandstone in terms of particle size distribution, mineralogy, strength, porosity and permeability. Cementation method using 10% sodium silicate solution reacting with CO_2 was chosen, and the commercial sand is used as a sand material. The sandstone diagenesis was simulated in the laboratory as follows: For a 10% sand/cement ratio, we mixed 23 kg quartz sand with 2.3 kg sodium silicate solution and then placed the mixture into the HPCS cell in 3 layers. The inner surface of the cell and the bottom plate was covered with filter paper to protect inlet ports from sand particles before placing the sample. Top of each layer was scratched before the next layer was placed to reduce bedding effect. After that, the top cap was installed. The top cap consists of two parts (Figure 11): the inverted T-shaped loading column and the coupler with the internal threads resting on the base of the loading column. The base of the loading column ensures uniform axial deformation of the sample. The upper part of the cell has external threads and the coupler of the top cap is screwed on it. Thus, the loading column is secured on top of the sample and sufficient water sealing is achieved.

A mobile overhead crane is used to navigate the top cap (Figure 12a). The mass of the hooked top cap is regulated by means of the scale and the spring to reduce the load on the threads otherwise the heavy mass of the top cap may damage the threads (Figure 12b).

Figure 11. Top cap.

Figure 12. The features of the top cap installing.

Once the top cap is placed, the cell is rolled under the frame. We started lifting the cell at 5 mm/min rate displacement control mode until there was a 2-3 mm gap between the top plunger and the frame. Then we switch to the stress control mode at 5 kPa/min up to the required vertical stress and maintained the stress for 12 hours to complete the consolidation. Low stress rate allows us to observe the point at which the top plunger touches the frame and the sample started to feel

the axial stress. This corresponds to the point when radial stress starts to increase. Difference between the displacement value at this point and the end of consolidation is used to calculate the axial strain during the consolidation. Also, the sample porosity was estimated from the final sample dimensions and the total mass of the sand-cement mixture. The low stress rate also provides slow and uniform consolidation. Once the consolidation is finished, CO_2 was injected into the sample and was allowed to circulate 20 minutes at 0.5 MPa pressure to activate the chemical process of cementation and create the artificial sandstone. This consolidation stress was kept constant at all stages except perforation.

The sample is saturated by flushing water through it from the bottom to the top using a constant 50 kPa inlet pressure for 24 hours. The flow rate during the flushing was used to calculate the initial permeability of the intact sample, assuming an isotropic condition. Darcy's equation for the water flow through a porous cylindrical sample can be written as:

$$q_w = \frac{-kA\Delta p}{\mu L} \tag{18}$$

where q_w is a water flow rate at 50 kPa inlet pressure; A – cross-section area of the sample; μ – water viscosity, L – sample height; Δp = 50 kPa – applied drawdown as inlet pressure is 50 kPa and outlet is open to the atmosphere; k – permeability of the sample.

After the saturation stage, the specimen was unloaded and moved out of the loading position (using the supporting frame (3)) such that a perforation tunnel was created by drilling a 14 mm diameter cylindrical hole into the centre of the top surface with the top cap in place. Figure 13 shows the sample surface a) before cementation; b) after cementation; c) after perforation.

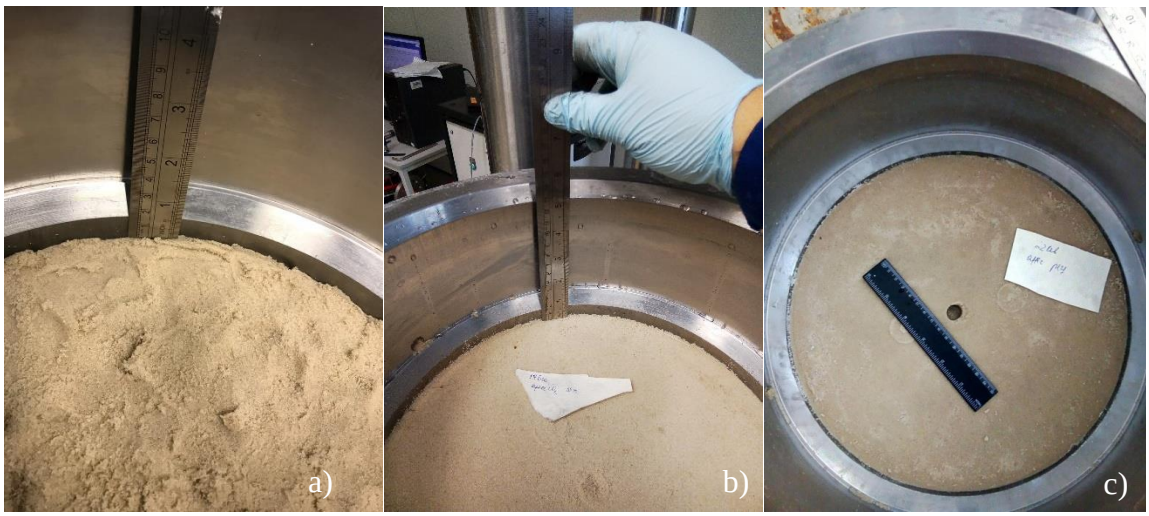

Figure 13. Sample surface: a) before cementation; b) after cementation; c) after perforation.

The sample was then returned to the loading position and the consolidation stress was again applied to the sample. This time stress rate was set to a higher value of 50 kPa/min which did not affect the sample properties as it already had been compressed to the consolidation stress value. Once the target stress value was reached, a vertical flow was applied to remove the perforation debris. It was observed that some debris appeared at the outlet at 0.9 l/min. However, a minimum of 2 l/min flow rate was required for the debris to be completely washed out of the sample. The

total mass of the debris was estimated from the dimensions of the hole, which is 52 g for ID = 14 mm hole.

Sand production experiments were conducted on the perforated sample with the flow diagram as shown in Figure 14. The cemented sample confined inside the cell from the previous steps was compressed vertically to a target stress value. Radial flow occurs as water is injected from the sides of the sample. Water and sometimes sand is observed to flow from the outlet on the top plunger and go to a system of the sieve and high accuracy scale to filter and measure the amount of produced sand particles in the flow. The produced sand data is recorded regularly until a steady state is achieved for the liquid flow and sand production wanes. Cleaned water returns to the fluid tank for further circulation.

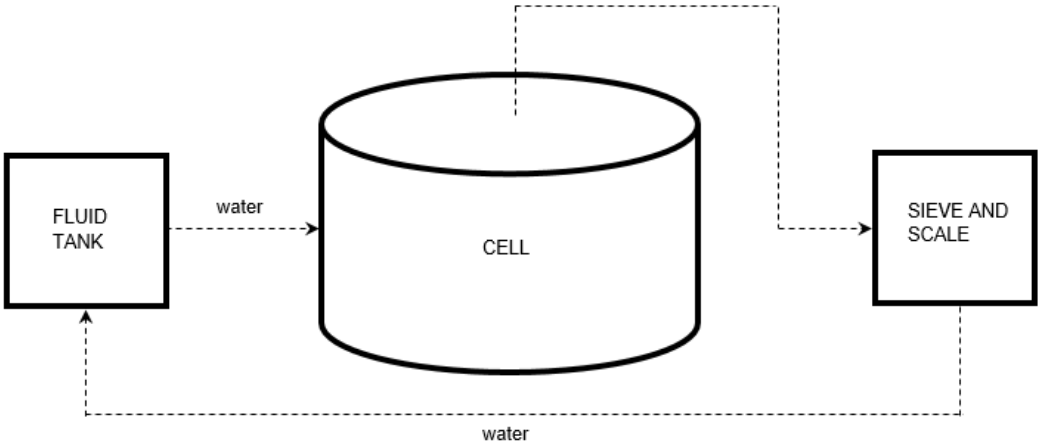

Figure 14. Flow diagram of the sand production experiment.

3.2 Sand production experimental results

The intact sample is characterized by an initial porosity of 38% and an initial permeability of 207 mD. The experiments were conducted at different axial stresses of 1 MPa to 5 MPa. The tests were attempted to replicate the transient sand production in the field. For a drawdown pressure and a corresponding produced flow rate, an initial sand burst is usually observed which is followed by a gradual decrease of the sand rate toward a negligible value. A subsequent increase of the flow rate may trigger another smaller burst of sand and then it wanes again. For each drawdown in the laboratory, the transient flow usually occurred approximately in the first 10 mins, which was followed by another 30 mins of the steady-state flow. At each stress stage different drawdowns were applied (Table 1). To apply a drawdown pressure, the inlet pressure was first increased to the required value through the control of the pump unit, while the outlet valve was closed. The no-flow condition was maintained for the fluid pressure to stabilize until the outlet pressure sensor shows the same value as the inlet pressure, and the outlet valve was opened to activate the flow. The flow was maintained for about 40 minutes until no sand was observed. The perforation debris of 52 g was collected in the first stage C1 using a minimum lifting flow rate of 2 l/min. No additional sand was observed at stages of 1 MPa and 2 MPa axial stress. On the other hand, sand was produced at stresses 3 MPa, 4 MPa and 5 MPa (Table 1).

Table 1. Sand production experimental results.

Test stages	Axial stress (kPa)	Radial stress 1 (kPa)	Radial stress 2 (kPa)	Drawdown (kPa)	Flow rate (l/min)	Average permeability (D)	Coefficient n (min/l)	Sand mass (g)
C1	1000	485	481	200	0.90	0.178	0.14	0
				400	1.56	0.157	0.14	0
				600	2.04	0.144	0.14	52
				800	3.00	0.120	0.14	0
C2	2000	696	1100	400	1.63	0.155	0.14	0
				800	2.70	0.128	0.14	0
C3	3002	1000	1505	800	2.50	0.120	0.16	0.854
				1000	2.87	0.108	0.16	0.585
C4	4000	1270	1625	800	2.36	0.112	0.20	6.652
				1000	2.76	0.099	0.20	3.254
C5	5003	1589	1940	1200	2.70	0.084	0.26	6.031
				1400	2.93	0.075	0.26	5.560

Average permeability at stages C1 and C2 was calculated using Eq.11 for the known drawdown and flow rate values and plotted in Figure 15.

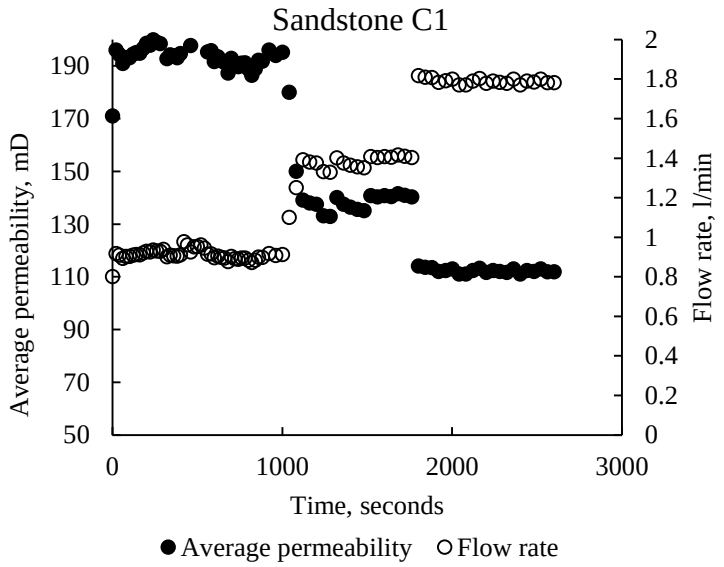

c)

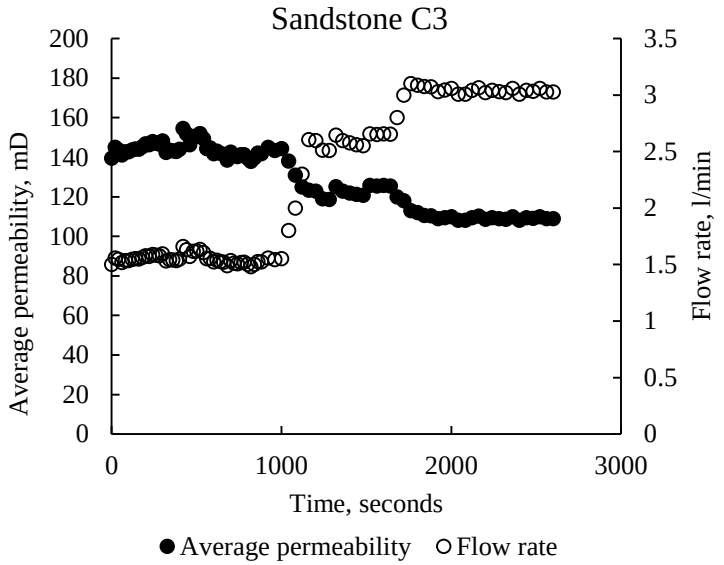

d)

Figure 15. Radial flow experimental results.

As can be seen from Figure 16, the average permeability of the sample keeps declining with the increased flow rate. According to the Eq.11, the average permeability value is affected by fluid viscosity, sample dimensions and hole radius. However, the sample radius and fluid viscosity do not change during the experiment. The sample contraction due to axial stress was negligible. The central hole does not enlarge at this stage because no sand production was indicated at these stages. The above discussions and observations lead to the conclusion that the only reason for average permeability to decrease is the formation of a low-permeable layer of plastic zone next to the hole wall. The average permeability k_{avg} of the perforated sample is plotted as a function of the flow rate (Figure 16).

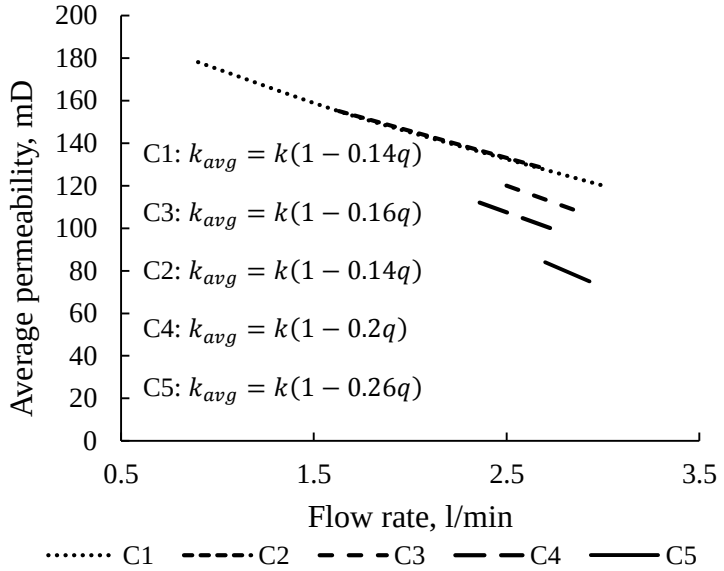

Figure 16. Average permeability in sand production experiments.

The linear relationships in Figure 16 can be approximated by a linear equation as follows:

$$k_{avg} = k(1 - nq) \tag{19}$$

where k_{avg} – average permeability of the sample, k – the intact zone permeability, q – flow rate, n – coefficient of proportionality. Note that since the dimension of permeability is mD and of flow rate is l/min, the value of the proportionality coefficient n is given in min/l. When necessary in the further calculation, the coefficient n can be converted to s/cm3 for consistency with other parameters.

Knowing the value of the average permeability as a function of the flow rate in Eq.15 and utilizing the equations of the shear failure model and the flow model, the plastic zone properties can be calculated for different drawdown and flow rate values: First, we record the drawdown and flow rate values at steady-state from the experiment. Then using Eq.11 we calculate average permeability. After that, we solve the system of two equations 9 and 10 for two unknowns k_p and R_p. Here k_p is average permeability of the plastic zone, which consists of high-permeable shear bands zone and compaction zone.

The plastic zone permeability is calculated with various flow rate values using the model and the results are shown in Figure 17. The symbols represent the data points of the real experiments and the actual measured flow rates. The lines represent the full range of the model's prediction behaviour, where the plastic zone permeability is calculated using assumed flow rate values outside the experimental range. For all stress levels and with an increasing flow rate, the plastic zone permeability decreases to a minimum value before it increases again at higher flow rate values.

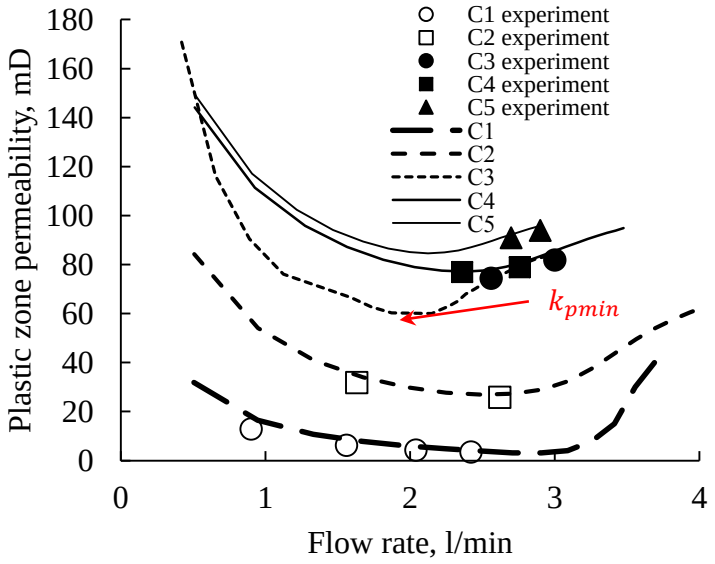

Figure 17. Plastic zone permeability results.

Sand production observed in the experiment need to satisfy two conditions: first, material failure happens, which produces particles that are weakly connected to the matrix and hence prone to the hydrodynamic erosion; and second, the fluid energy must be sufficient to bring the detached particles to the outlet. Despite the flow rate was higher than the minimum lifting flow rate of 2 l/min, no sand was collected in the experiments C1 and C2, but the same flow rates produced sands

in C3, C4, and C5. This implies that both conditions are necessary for sand production. Furthermore, sand production in Figure 17 occurs with an increase in the plastic zone permeability (solid points).

This is consistent with discussions on Figure 6, where sand production is associated with sand migration from the compaction zones to the shear bands zone and perforation hole.

Now we will analyze experimental results in terms of porosity change in the plastic zone. Let us examine experimental results C3 (Table 1) at 800 kPa drawdown. Table 2 lists the input parameters for the volume and sand rate calculations.

Table 2. Input parameters for the model calculations at 3MPa axial stress.

Parameter	Value
Inner hole radius, m	0.007
Outer radius, m	0.15
Drawdown, Pa	800 000
Fluid viscosity, Pa*s	0.001
Vertical stress, Pa	3 000 000
Horizontal stress, Pa	1 200 000
Flow rate, m^3/s	4.21×10^{-5}
Rock properties and sample dimensions	
Intact zone permeability, m^2	$0.207\cdot10^{-12}$
Average permeability, m^2	$0.120\cdot10^{-12}$
Permeability coefficient	1.449
Cohesive strength of the sample, Pa	120 000
Failure angle, degrees	64
Sample height, m	0.214
Sample diameter, m	0.15

We assume that maximum contraction takes place when the plastic zone permeability reaches its minimum value of 61 mD according to Figure 17 and corresponds to the state *A* which describes porosity and permeability distribution before sand production for sandstone C3 at drawdown and flow rates of 580 kPa and 2.1 l/min. State *B* shows porosity and permeability distribution after sand production at 800 kPa drawdown pressure for which k_p = 65 mD - an average value of the permeability across the plastic zone as in Eq.13.

k_0 value is found from the Kozeny-Carman relationship for intact porosity and permeability values:

$$207\ mD = k_0 \frac{0.38^3}{(1-0.38)^2} \Rightarrow k_o = 1.449$$

Solving the Eqs. 13 – 17 for the experimental results of sandstone C3 we can estimate porosity distribution at states *A* and *B* (Tables 3 and 4).

Table 3. Model results for state *A*.

R_{sb}^A	R_p^A	ϕ_{sb}^A	k_{sb}^A	ϕ_c^A	k_c^A	ϕ_p^A	k_p^A	q

m	m	-	mD	-	mD	-	mD	l/min
0.0104	0.0137	0.584	1668	0.2328	31	0.2796	61	2

In case some of the sand mass is trapped in the shear bands zone during transport from the compaction zone to the hole, porosity in the shear bands zone decreases, and only part of the transported sand is produced. In this case, the mass of the produced sand will depend on the amount of the sand trapped in the shear bands zone (Table 4):

Table 4. Model results for state *B*.

R_{sb}^B	R_p^B	ϕ_{sb}^{B*}	k_{sb}^B	ϕ_c^B	k_c^B	ϕ_p^B	k_p^B	q	m_s^{min}
m	m	-	mD	-	mD	-	mD	l/min	g
0.016	0.0194	0.536	1038	0.2018	18.7	0.2844	65	2.5	0.3
0.016	0.0194	0.537	1048	0.2018	18.7	0.2844	65	2.5	0.5
0.016	0.0194	0.538	1060	0.2018	18.6	0.2844	65	2.5	0.8
0.016	0.0194	0.54	1078	0.2017	18.6	0.2844	65	2.5	1.4
0.016	0.0194	0.545	1138	0.2016	18.6	0.2844	65	2.5	3
0.016	0.0194	0.556	1268	0.2013	18.5	0.2844	65	2.5	6
0.016	0.0194	0.577	1558	0.2009	18.4	0.2844	65	2.5	12
0.016	0.0194	0.584	1668	0.2008	18	0.2844	65	2.5	14

According to the experimental results we produced 0.854 g sand at 2.5 l/min during the first ten minutes and stopped the experiment as no sand was observed after forty minutes of the experiment. On the other hand, Table 4 shows us that we could have produced a maximum of 14 g sand. This means that a time column is missing in Table 4. Thus, ten minutes is required for fluid flow to transport sand particles from the compaction zone to the shear bands zone to increase its porosity from 0.23 to 0.54, and also to transport 0.8 of sand mass to the perforation hole. The fact that we didn't observe sand for the rest thirty minutes indicates that further sand migration was very slow and we stopped the experiment before producing all the producible sand predicted by the model, which is 14 g. Continuous sand measurement technique could be a good solution to this problem in future studies, but in the current research, the sand was not measured continuously. In addition, the microcamera pictures which were taken inside the hole after the test indicate that there are some sand particles accumulated at the hole bottom (Figure 18). This may be due to slippage of the detached single particles into larger clusters so that the applied flow rate was not enough to lift them to the surface.

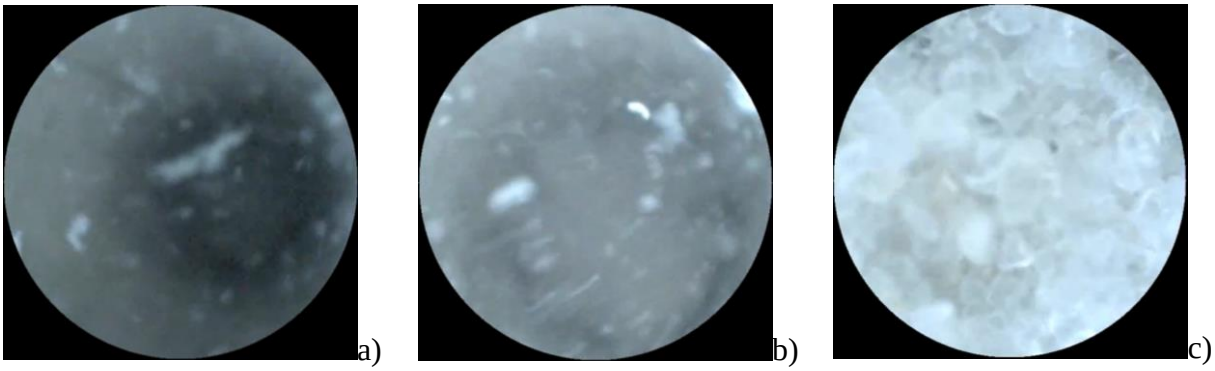

Figure 18. Sand particles accumulated at the bottom of the hole captured at different height: a) from the top part of the hole; b) from the middle part of the hole; c) from the bottom of the hole.

3.3 Transient sand production prediction

New findings on the porosity and permeability distribution discussed above will be used to modify the existing transient sand production prediction models to demonstrate the importance of the plastic zone properties. The first model was suggested by Geilikman et al. (1994), extended by van den Hoek and Geilikman (2003) and considers sand production as a viscoplastic granular flow. The model states that the sand is produced from the plastic zone around a hole, and this plastic zone has a higher porosity than the intact zone due to sand production. The second model is based on the studies by Vardoulakis et al., (1996b); Skjaerstein et al., (1997a); Papamichos et al., (2001) and studies the erosion behaviour of the solids due to fluid flow. The authors introduced a sand production coefficient λ to describe the erosional behaviour of sand matrix. In the original model (Papamichos et al., 2001), the sand is produced from the intact zone and the intact zone porosity is used as an initial value of the porosity in the calculations.

On the other hand, we have shown above that the plastic zone has lower permeability and porosity compared to the intact zone, and is composed of two subzones: high-permeable shear bands zone and low-permeable compaction zone. Thereby we make modifications to the models presented by van den Hoek and Geilikman (2003) and Papamichos et al. (2001) in terms of the plastic zone radius, permeability and porosity according to our new findings. Thus, we propose that sand is produced from the compaction zone when its porosity and permeability increase from ϕ_c^A to ϕ_{sb}^B and from k_c^A to k_{sb}^B, respectively, and the plastic zone radius changes from R_{sb}^A to R_{sb}^B.

Sanding rate is calculated using two modified models and compared to the experimental results for the test at 3 MPa axial stress and drawdown of 800 kPa. Table 5 presents input parameters for the sanding rate calculations and Figure 19 shows the model results.

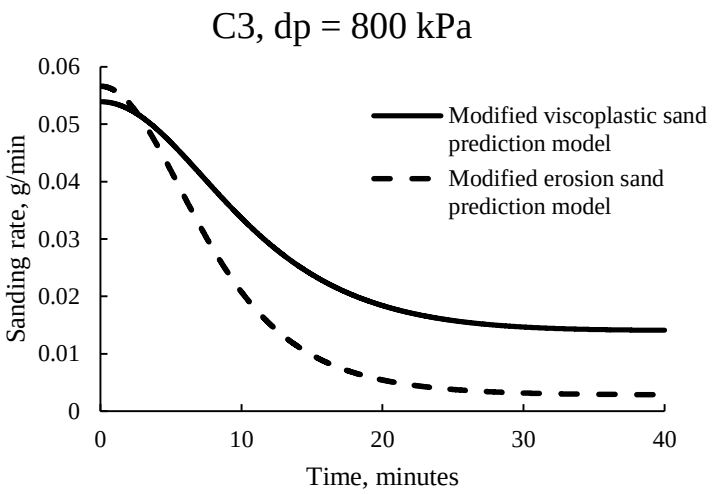

Figure 19. Transient sand prediction model results for sample C3 at 800 kPa drawdown.

Table 5. Input parameters for the sanding rate calculations at 3MPa axial stress.

Parameter	Notation	Value
Initial radius of the shear bands zone, m	R_{sb}^{A}	0.0104
Outer radius, m	R_o	0.15
Current radius of the shear bands zone, m	R_{sb}^{B}	$R_{sb}^{A} + 0.0055 \cdot (1 - e^{-\frac{t^2}{10^6}})$
Drawdown, Pa	$p_o - p_i$	800 000
Fluid viscosity, Pa*s	μ	0.001
Effective radial stress at hole wall, Pa	σ_i	0
Radial stress at infinity, Pa	σ_∞	1 200 000
Rock properties and sample dimensions		
Compaction zone permeability before sand production, m^2	k_c^A	$0.031 \cdot 10^{-12}$
Compaction zone permeability after sand production, m^2	k_{sb}^B	$1.668 \cdot 10^{-12}$
Compaction zone porosity before sand production, -	ϕ_c^A	0.23
Compaction zone porosity after sand production, -	ϕ_{sb}^B	0.58
Intact zone UCS, MPa	UCS_i	1
Plastic zone UCS, MPa	UCS_p	0
Friction angle, degrees	ϕ	38
Dilatancy angle, degrees	ψ	8
Viscoplastic viscosity, Pa·s	η	10^{11}
Sand production coefficient, m^{-1}	λ	$3 \cdot 10^{-5}$ - $3 \cdot 10^{-4}$
Poroelastic coefficient, -	γ_p	0.9
Sample height, m	L	0.214

As can be seen from Figure 19, the peak rate of the results for the modified models is comparable. However, the tail of the curve is far above zero for the modified viscoplastic sand prediction model. Total sand mass produced during the first forty minutes can be estimated by calculating the area under the sanding rate curve $m_s^{viscoplastic}(40) = 1\ g$ for the modified viscoplastic model and $m_s^{erosion}(40) = 0.588\ g$ for the modified erosion model. Both results are more than the sand mass produced during the experiment. In addition, at this calculated sanding rate it would require 16 hours for the modified viscoplastic model and 83 hours for the modified erosion model to produce all the theoretically producible sand mass which is 14 g.

For a clearer view of the model performance, let us conduct all the calculations in the previous and current chapters for all experiments. Table 6 shows the calculation results for all experiments.

Table 6. Experimental and modelling results of the sand production.

Axial stress, MPa	Draw down, kPa	Sand mass from the experiment, g	Theoretical total sand mass, g	Viscoplastic model			Erosion model		
				Sand mass from in 40 mins, g	Relative error, %	Time to produce all sand, hours	Sand mass from in 40 mins, g	Relative error, %	Time to produce all sand, hours
3	800	0.854	14	1.0068	15	16	0.588	45	83
3	1000	0.585	43	0.4	46	27	0.573	2	238
4	800	6.652	36	5.8901	13	5	4.25	57	20
4	1000	3.254	130	3.023	8	55	4.1	21	81
5	1200	6.031	143	5.3243	13	43	5.65	7	61
5	1400	5.56	148	4.5602	22	38	5.3	5	63

As can be seen from Table 6, the modified sanding rate prediction models mostly underestimate the produced sand mass. The relative error is as high as 57% with the smallest value being between 2% and 8%. In each model, we used the same model coefficients (such as formation viscosity or sand production coefficient) as in the original model. But those constants may not be applicable for our sample and this may result in higher errors. To estimate the significance of the modification based on the plastic zone properties, we compare the relative error of the original models by van den Hoek and Geilikman (2003) and Papamichos et al. (2001) and the current modified model. As can be seen from Table 6, the performance of the modified models is better than the original models despite their moderate to high error values. The original models predicted sand masses 2-3 times greater than that from the experiment. The porosity changes from 0.38 to 0.6 in the original models, while in the modified models it changes from around 0.2 to 0.6. As can be seen, the difference is not that large. On the other hand, plastic zone radius change is considerably different in the original models and the modified models. Therefore, plastic zone properties should be accurately defined for better predictions.

Table 7. Comparison between the original models (Papamichos et al., 2001; Paul Jacob van den Hoek & Geilikman, 2003) and the modified models (current study).

Axial stress, MPa	Drawdown, kPa	Sand mass from the experiment, g	Relative error, %			
			Viscoplastic model	Modified viscoplastic model	Erosion model	Modified erosion model
3	800	0.854	185	15	73	45
3	1000	0.585	193	46	78	2
4	800	6.652	122	13	56	57
4	1000	3.254	81	8	58	21
5	1200	6.031	202	13	104	7
5	1400	5.56	178	22	106	5

For further assessment of the modified models, the sanding rate data from the weak sandstone reservoir was used. The following section presents the field validation results of the modified viscoplastic model as the model was more convenient to adapt for the field conditions than the modified erosion model.

3.4 Field data validation

The produced sand data from a heavy oil sandstone reservoir in Kazakhstan were used to validate the sand production model with the updated zone properties. Assumptions of the model apply for the wells which meet the following set of criteria:

1) The well produces from a single or a couple of homogeneous production layers;
2) The thickness of the producing layer is more than 2 m;
3) Pay-to-gross ratio of the producing layer should be above 80%;
4) Water cut of the produced liquid is less than 10%;

As the model is developed for different production stages of constant flow rate, additional criteria can be added:

5) The well produces at an approximately constant flow rate.

Screening 3000 production wells from the field, 40 wells that satisfy all conditions above were chosen for the validation of the model. The field data consist of average values of fluid rate, sand rate, and bottom-hole pressure per month. The comparison of the model and field data was conducted in terms of the magnitude of the peak sand production rate and the pattern of the sanding behaviour.

The prediction of a specific well producing from Horizon B is explained in detail here as an example. The effective thickness of the interval is 2.9 m at 235 m depth. Vertical stress at the outer boundary is $\sigma_v = 5.3$ MPa at 221 m. Horizontal stresses at the outer boundary are equal and taken as $\sigma_H = \sigma_h = 0.4 \cdot \sigma_v$ = 2.12 MPa. Current reservoir pressure is 2 MPa, bottom-hole pressure is 0.77 MPa.

The model in this study was developed for a vertical cavity. For a horizontal perforation of a vertical well, the stress distributions can be modified with transformation formulas (Fjaer et al., 1993) for the application of the model. Sand rate is calculated for a single perforation tunnel, and the total sand rate of the well is found by multiplying the result by the number of perforations. The same geometry is assumed the calculation of a single perforation here as the perforation procedure was identical throughout the field with a density of 16 shots per meter and phasing of 90°. This implies that the vertical distance between two adjacent horizontal perforations is 0.25 m. Half distance between the adjacent perforations is taken as an outer boundary, i.e. R_o = 0.125 m. Gun passport suggests the average diameter and length of the perforation tunnel as 2Ri = 0.0166 m and L = 2 m, respectively.

Field data on porosity and permeability for this well are absent, but the values for horizon B are in the following ranges: porosity – from 0.31 to 0.39; permeability – from 89 mD to 1050 mD. The initial porosity and permeability of the field hence can be assumed as the same as in the sand production experiments: 0.38 and 207 mD, respectively. Similarly, cohesion and friction angle of the reservoir rock are not known and assumed as 0.12 MPa and 64° as in the experiment. All the input data are shown in Table 8.

Table 8. Input data for field validation. A well producing from horizon B, central part.

	Parameter	Unit	Value
Pressures	Fluid pressure at the outer boundary, p_o	MPa	2
	Fluid pressure at the borehole, p_w	MPa	0.77
	Vertical stress at the boundary, σ_v	MPa-	5.3
	Maximum and minimum horizontal stresses at the boundary, $\sigma_H = \sigma_h$	MPa	2.12
	Depth	m	235
Perforation dimensions	Perforation radius, R_i	m	0.0083
	Perforation length, L	m	2
	Outer boundary radius, R_o	m	0.125
	Number of perforations, N		46
Fluid properties	Fluid rate	t/day	7.5
	Fluid viscosity	Pa·s	0.55

The production from the well was around 7.5 t/day for 36 months with water cut below 10%. The associated sand rate of the well is compared to the predicted values as shown in Figure 20. It shows that the model captures well the peak sand rate and the cease of sanding in the steady-state, although the change in the field data appears more gradually and there is a persistent fluctuation in the field data. The main questions the prediction model should answer are that how much sand we are going to produce at the peak of the sand production and how long this peak time lasts so that the surface facilities are arranged accordingly to handle the produced sand. Therefore the model performance can be considered as satisfactory and produces valuable information.

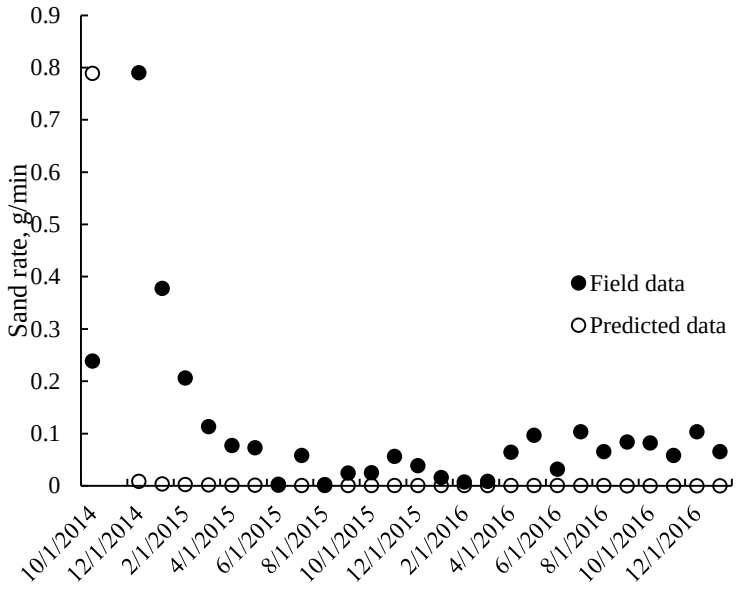

Figure 20. Field data validation of the model.

Similar calculations were conducted for all 40 wells. The wells were producing from five horizons, A1, A2, B, G and V. Producing depths of the horizons vary from 260 m to 530 m due to the specific structure of the field, and the exact numbers are known for each well. Single values of cohesion and friction angle, porosity and permeability as in the experiments were used for all 40 wells. Perforation characteristics were assumed to be the same for all wells, however, the number of perforations varied depending on the thickness of the producing interval.

Figure 21 shows the model performance for the prediction of the peak sand rate for all 40 wells, where the ordinate indicates the number of wells of which the prediction falls within a particular error range. Error is calculated as a ratio of the predicted maximum rate to the maximum field rate. If the ratio is higher than the unit, then the model overpredicts by the amount above one multiplied by 100. Similarly, if the ratio is less than one, then the model underpredicts by the difference between the ratio and one multiplied by 100.

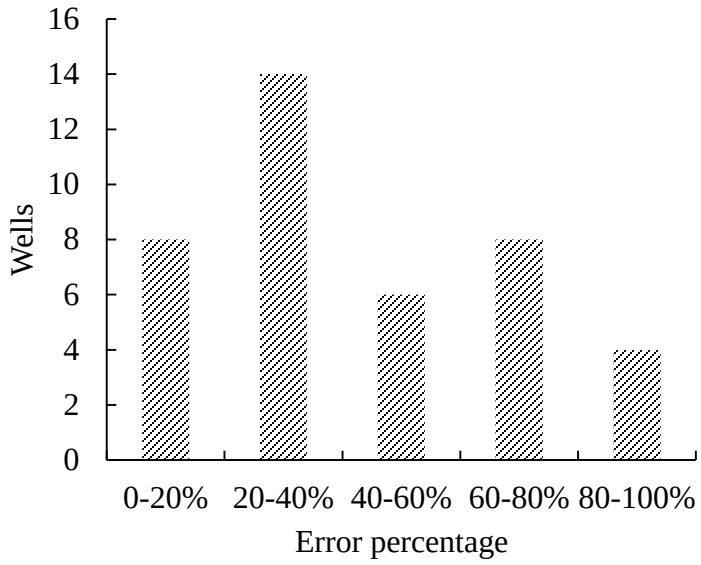

Figure 21. The model performance for 40 wells.

Eight wells out of the total forty wells were predicted within 20% error, which is considered as a sufficient level of accuracy. Most wells were predicted with error within 20%-40% of the actual data. The best predicted eight wells were producing from Horizon B in the central part of the field, the same horizon as the well in Figure 20, where the reservoir pressure does not exceed 2 MPa. The results suggest that material properties and fluid properties used in the model can be the most applicable to this location. The field conditions, however, may vary for both the reservoir rock and the fluid properties and this is not accounted for in the prediction of the 40 wells.

4 Conclusion

This study analytically and experimentally investigates the role of plastic zone permeability and porosity on the prediction of sand volume and rate. Large scale sand production experiments were conducted using a customized High-Pressure Consolidation System. The existing sand prediction models were upgraded with new information on the plastic zone permeability to achieve a semi-analytical prediction model for the sand production from a hollow cylinder weak artificial sandstone under radial flow. The obtained model was validated using the sand data from a weak sandstone reservoir. The current study was conducted to show the importance of the plastic zone permeability and porosity distribution around a perforation hole. The plastic zone in weak sandstones is composed of two subzones with different porosity and permeability values: high-permeable shear bands zone and low-permeable compaction zone. Average permeability and porosity in the plastic zone are less than that of the intact zone. The existing sand prediction models can be updated with the plastic zone properties for better performance. The results indicate the significance of the decreased plastic zone porosity and permeability in the sand production prediction, and, the model performance is positive for further development and improvement in the laboratory and the real applications.

Nomenclature

k	Intact zone permeability
k_0	Permeability coefficient
k_{ave}	Average permeabiliy of the sample
k_c	Permeability of compaction zone
k_p	Permeability of plastic zone
k_{sb}	Permeability of shear bands zone
L	Perforation length
η	Viscoplastic viscosity
n	Proportionality coefficient
N	Number of perforations
p_o	Fluid pressure at boundary
p_i	Fluid pressure at wellbore wall
p_p	Fluid pressure at plastic/elastic zones boundary
Δp	Drawdown
p’	The mean effective stress
q	Fluid flow rate
q_p	Fluid flow rate across plastic zone
q_{avg}	Average fluid flow rate across the sample
q	Deviatoric stress
r	Radial distance from hole axis
R_i	Radius of perforation tunnel
R_o	Radius of outer boundary for perforation tunnel
R_c	Radius of compaction zone
R_p	Radius of plastic zone
R_{sb}	Radius of shear bands zone
S_0	Inherent shear strength
t	Time
α	Failure angle
φ	Friction angle
ψ	Dilatancy angle
γ	Poroelastic coefficient
μ	Fluid viscosity
ν_{fr}	Drained poisson’s ratio
ρ_s	Density of sand grains
σ_{1e}’	Effective maximum principal stress
σ_{3p}’	Effective minimum principal stress
σ_h	Minimum horizontal stress
σ_H	Maximum horizontal stress
σ_r	Radial stress at distance r
σ_v	Far-field vertical overburden stress
σ_z	Axial stress at distance r
σ_θ	Tangential stress
ϕ	Porosity in the intact zone
ϕ_c	Porosity in the compaction zone
ϕ_p	Porosity in the plastic zone
ϕ_{sb}	Porosity in the shear bands zone

Acknowledgments

This research was sponsored by Nazarbayev University (research grant No. SOE2015004) and Ministry of Education and Science of the Republic of Kazakhstan (research grant No. AP08052762). The authors would like to thank the operating company for the provided field data.

References

Al-Shaaibi, S. K., Al-Ajmi, A. M., & Al-Wahaibi, Y. (2013). Three dimensional modeling for predicting sand production. *Journal of Petroleum Science and Engineering*, *109*, 348–363. https://doi.org/10.1016/j.petrol.2013.04.015

Araujo, E. F., Alzate, G. A., Arbelaez, A., Peña, S., Cardona, A., & Naranjo, A. (2014). Analytical Prediction Model of Sand Production Integrating Geomechanics for Open Hole and Cased – Perforated Wells. *Society of Petroleum Engineers*. https://doi.org/10.2118/171107-MS

Arora, D. S., & Sharma, M. M. (2000). Nature of the compacted zone around perforation tunnels. *Proceedings - SPE International Symposium on Formation Damage Control*, (10), 113–124.

Bratli, R. K., & Risnes, R. (1981). Stability and Failure of Sand Arches. *SPE Journal*. https://doi.org/10.2118/8427-PA

Carman, P. C. (1939). Permeability of saturated sands, soils and clays. *The Journal of Agricultural Science*, *29*(2), 262–273. https://doi.org/10.1017/S0021859600051789

Cerasi, P., Papamichos, E., & Stenebråten, J. F. (2005). Quantitative Sand-Production Prediction: Friction-Dominated Flow Model. In *SPE Latin American and Caribbean Petroleum Engineering Conference*.

Cuss, R. J., Rutter, E. H., & Holloway, R. F. (2003). Experimental observations of the mechanics of borehole failure in porous sandstone. *International Journal of Rock Mechanics and Mining Sciences*, *40*(5), 747–761. https://doi.org/10.1016/S1365-1609(03)00068-6

Daigle, H., Rasromani, E., & Gray, K. E. (2017). Near-wellbore permeability alteration in depleted, anisotropic reservoirs. *Journal of Petroleum Science and Engineering*, *157*(April), 302–311. https://doi.org/10.1016/j.petrol.2017.07.046

Dobereiner, L., & Freitas, M. H. De. (1986). Geotechnical properties of weak sandstones. *Géotechnique*, *36*(1), 79–94. https://doi.org/10.1680/geot.1986.36.1.79

Fattahpour, V., Moosavi, M., & Mehranpour, M. (2011). An experimental rock mechanics investigation for sand production in oil fields. *45th US Rock Mechanics / Geomechanics Symposium*. Retrieved from http://www.scopus.com/inward/record.url?eid=2-s2.0-82555204547&partnerID=tZOtx3y1

Fattahpour, V., Moosavi, M., & Mehranpour, M. (2012). An experimental investigation on the effect of rock strength and perforation size on sand production. *Journal of Petroleum Science and Engineering*, *86–87*, 172–189. https://doi.org/10.1016/j.petrol.2012.03.023

Fjaer, E., Holt, R. M., Horsrud, P., Raaen, A. M., & Risnes, R. (1993). *Petroleum related rock mechanics* (2nd ed., Vol. 30). Elsevier B.V. https://doi.org/10.1016/0148-9062(93)92632-Z

Fuh, G., & Morita, N. (2013). Sand productino prediction analysis of heterogeneous reservoirs for sand control and optiaml well completion design. *International Petroleum Technology*

Conference. https://doi.org/10.2523/16940-MS

Geilikman, M. B., Dusseault, M. B., & Dullien, F. A. (1994). Sand Production as a Viscoplastic Granular Flow. *SPE Symposium on Formation Damage Control*. https://doi.org/10.2118/27343-ms

Goshtasbi, K., Elyasi, A., & Naeimipour, A. (2013). Numerical assessment of the mechanical stability in vertical, directional and horizontal wellbores. *International Journal of Mining Science and Technology*, *23*(6), 937–942. https://doi.org/10.1016/j.ijmst.2013.11.010

Han, G., Dusseault, M. B., & Cook, J. (2002). Quantifying Rock Capillary Strength Behavior in Unconsolidated Sandstones. *Proceedings of the SPE/ISRM Rock Mechanics in Petroleum Engineering Conference*, 171–180.

Han, Gang, & Dusseault, M. B. (2003). Description of fluid flow around a wellbore with stress-dependent porosity and permeability. *Journal of Petroleum Science and Engineering*, *40*(1–2), 1–16. https://doi.org/10.1016/S0920-4105(03)00047-0

Han, Gang, Shepstone, K., Harmawan, I., Er, U., Jusoh, H., Lin, L. S., … Diessl, J. (2011). A Comprehensive Study of Sanding Rate From a Gas Field: From Reservoir to Completion, Production, and Surface Facilities. *Spe Journal*, *16*(2), 463–481. https://doi.org/10.2118/123478-PA

Hayavi, M. T., & Abdideh, M. (2017). Establishment of tensile failure induced sanding onset prediction model for cased-perforated gas wells. *Journal of Rock Mechanics and Geotechnical Engineering*, *9*(2), 260–266. https://doi.org/10.1016/j.jrmge.2016.07.009

Holt, R. M. (1990). Permeability Reduction Induced by a Nonhydrostatic Stress Field, (December).

Kessler, N., Wang, Y., & Santarelli, F. J. (1993). A Simplified Pseudo 3D Model To Evaluate Sand Production Risk in Deviated Cased Holes. *SPE Annual Technical Conference and Exhibition*. https://doi.org/10.2118/26541-ms

Khamitov, F., Minh, N. H., & Zhao, Y. (2020a). Microscopic numerical modelling of perforation damage and sand production in weak sandstone formation. *Under Review*.

Khamitov, F., Minh, N. H., & Zhao, Y. (2020b). Microscopic numerical modelling of perforation damage and sand production in weak sandstone formation. *Under Review*, 1–23.

Kozeny, J. (1927). Uber Kapillare Leitung Des Wassers in Boden: Sitzungsberichte der Wiener Akademie der Wissenschaften.

Morita, N., Whitfill, D. L., Massie, I., & Knudsen, T. W. (2007). Realistic Sand-Production Prediction: Numerical Approach. *SPE Production Engineering*, *4*(01), 15–24. https://doi.org/10.2118/16989-pa

Morita, N., Whitfill, D. L., Massle, I., & Knudsen, T. W. (1989). Realistic Sand-Production Prediction: Numerical Approach.pdf. *SPE Production Engineering*, *4*(1), 15–24.

Nouri, A., Vaziri, H. H., Belhaj, H. A., & Islam, M. R. (2006). Sand-Production Prediction: A New Set of Criteria for Modeling Based on Large-Scale Transient Experiments and Numerical Investigation. *SPE Journal*, *11*(02), 227–237. https://doi.org/10.2118/90273-pa

Papamichos, E., & Furui, K. (2013). Sand production initiation criteria and their validation. *47th US Rock Mechanics/Geomechanics Symposium*.

Papamichos, E., & Furui, K. (2019). Analytical models for sand onset under field conditions. *Journal of Petroleum Science and Engineering*, *172*(February 2018), 171–189. https://doi.org/10.1016/j.petrol.2018.09.009

Papamichos, E., Skjaerstein, A., & Tronvoll, J. (2000). A volumetric sand production experiment. *Pacific Rocks*, 303–310.

Papamichos, E., Vardoulakis, I., Tronvoll, J., & Skjaerstein, A. (2001). Volumetric sand production model and experiment. *International Journal for Numerical and Analytical Methods in Geomechanics*, *25*(8), 789–808. https://doi.org/10.1002/nag.154

Raghavan, R., Chin, L. Y., & Company, P. P. (2002). Productivity Changes in Reservoirs With Stress-Dependent Permeability. In *SPE Annual Technical Conference and Exhibition*.

Risnes, R., Bratli, R. K., & Horsrud, P. (1982). Sand Stresses Around a Wellbore. *Society of Petroleum Engineers Journal*, *22*(06), 883–898. https://doi.org/10.2118/9650-pa

Sarda, J.-P., Ferfera, F. M. R., Vincké, O., Boutéca, M., & Longuemare, P. (1988). EXPERIMENTAL STUDY OF THE STRESS PATHS INFLUENCE ON MONOPHASIC PERMEABILITY EVOLUTION. In *Society of Core Analysts, International Symposium* (pp. 14–16).

Shabdirova, A., Minh, N. H., & Zhao, Y. (2019). A sand production prediction model for weak sandstone reservoir in Kazakhstan. *Journal of Rock Mechanics and Geotechnical Engineering*, (xxxx). https://doi.org/10.1016/j.jrmge.2018.12.015

Skjaerstein, A., Stavropoulou, M., Vardoulakis, I., & Tronvoll, J. (1997). Hydrodynamic erosion; A potential mechanism of sand production in weak sandstones. *International Journal of Rock Mechanics and Mining Sciences*, *34*(3–4). https://doi.org/10.1016/S1365-1609(97)00190-1

Skjaerstein, Anne, Tronvoll, J., Santarelli, F. J., & Joranson, H. (1997). Effect of water breakthrough on sand production: Experimental and field evidence. *Proceedings - SPE Annual Technical Conference and Exhibition, Pi*, 565–575.

Tovar, J., Salazar, A., & Salazar, N. (2007). Integrating drilling and geomechanical damage in sandstone reservoirs: Identification, quantification, and removal. *SPE - European Formation Damage Conference, Proceedings, EFDC*, *1*, 330–337.

Tronvoll, J., & Fjær, E. (1994). Experimental study of sand production from perforation cavities. *International Journal of Rock Mechanics and Mining Sciences And*, *31*(5), 393–410. https://doi.org/10.1016/0148-9062(94)90144-9

van den Hoek, P.J., Hertogh, G. M. M., Kooijman, A. P., de Bree, P., Kenter, C. J., & Papamichos, E. (2007). A New Concept of Sand Production Prediction: Theory and Laboratory Experiments. *SPE Drilling & Completion*, *15*(04), 261–273. https://doi.org/10.2118/65756-pa

van den Hoek, Paul Jacob, & Geilikman, M. B. (2003). Prediction of Sand Production Rate in Oil and Gas Reservoirs. *SPE Annual Technical Conference and Exhibition*. https://doi.org/10.2118/84496-MS

Vardoulakis, I., Stavropoulou, M., & Papanastasiou, P. (1996). Hydro-mechanical aspects of the sand production problem. *Transport in Porous Media*, *22*(2), 225–244. https://doi.org/10.1007/BF01143517

Wang, H., & Sharma, M. M. (2017). The Role of Elasto-Plasticity in Cavity Shape and Sand Production in Oil and Gas Wells. *SPE Annual Technical Conference and Exhibition*, (2000). https://doi.org/10.2118/187225-MS

Wang, Y., & Dusseault, M. B. (2010). Sand Production Potential Near Inclined Perforated Wellbores. https://doi.org/10.2118/96-70

Weingarten, J. S., & Perkins, T. K. (2007). Prediction of Sand Production in Gas Wells: Methods and Gulf of Mexico Case Studies. *Journal of Petroleum Technology*, *47*(07), 596–600. https://doi.org/10.2118/24797-pa

Wu, B., & Choi, S. K. (2012). Effect of Mechanical and Physical Properties of Rocks on Post-Failure Post Cavity Development – Experimental and Numerical Studies. *The 46th US Rock Mechanics/Geomechanics Symposium*.

Wu, B, Petroleum, C., Mohamed, N. A., Services, S., Bhd, S., Viswanathan, C., … Bhd, S. (2006). SPE 101087 An Integrated Wellbore Stability and Sand Production Prediction Study for a Multi-Field Gas Development.

Wu, Bailin, Choi, S. K., Denke, R., Barton, T., Viswanathan, C., Lim, S., … Shaffee, S. (2016). A New and Practical Model for Amount and Rate of Sand Production. *Offshore Technology Conference*, 18.

Yan, M., Deng, J., Yu, B., Li, M., Zhang, B., Xiao, Q., & Tian, D. (2020). Comparative study on sanding characteristics between weakly consolidated sandstones and unconsolidated sandstones. *Journal of Natural Gas Science and Engineering*, *76*(December 2019), 103183. https://doi.org/10.1016/j.jngse.2020.103183

Yi, X. (2003). *Numerical and Analytical Modeling of Sanding Onset Prediction Numerical and Analytical Modeling of Sanding Onset Prediction*.

Zhu, W., & Wong, T. (1997). The transition from brittle faulting to cataclastic flow: Permeability evolution. *Journal of Geophysical Research: Solid Earth*, *102*(B2), 3027–3041. https://doi.org/10.1029/96jb03282

Declaration of interests

☒ The authors declare that they have no known competing financial interests or personal relationships that could have appeared to influence the work reported in this paper.

☒The authors declare the following financial interests/personal relationships which may be considered as potential competing interests:

No

Ainash Shabdirova
Minh Nguyen
Yong Zhao